ISSN 1540-7063 (PRINT)
ISSN 1557-7023 (ONLINE)

Integrative & Comparative Biology

Volume 58 Number 2 August 2018
academic.oup.com/icb

Integrative and Comparative Biology

Integrative and Comparative Biology, volume 58, number 2, pp. 261–275
doi:10.1093/icb/icy053

Society for Integrative and Comparative Biology

SYMPOSIUM

Shape, Size, and Structure Affect Obliquely Striated Muscle Function in Squid

Kari R. Taylor-Burt,[*] William M. Kier,[†] Julia Olszewski-Jubelirer[†] and Joseph T. Thompson[1,‡]

[*]Department of Organismic and Evolutionary Biology, Harvard University, Cambridge, MA 02138, USA; [†]Department of Biology, University of North Carolina, Chapel Hill, NC 27599, USA; [‡]Department of Biology, Franklin & Marshall College, P.O. Box 3003, Lancaster, PA 17604, USA

From the symposium "Spatial Scale and Structural Heterogeneity in Skeletal Muscle Performance" presented at the annual meeting of the Society for Integrative and Comparative Biology, January 3–7, 2018 at San Francisco, California.

[1]E-mail: joseph.thompson@fandm.edu

Synopsis Hollow, cylindrical body plans, and obliquely striated muscles are characteristic of soft-bodied invertebrates, and both affect the biomechanics of movement in these diverse animals. We highlight two different aspects of functional heterogeneity in obliquely striated muscles, one driven by animal shape and size and the other by the intrinsic mechanical properties of the fibers. First, we show how a hollow, cylindrical shape in the mantle of cephalopod molluscs causes a significant difference in muscle strain (defined as the change in length divided by resting length) across the mantle wall, and describe the implications of such "transmural gradients of strain" for the length–tension relationship of the obliquely striated muscles that power movements in these animals. We show that transmural gradients of strain increase in magnitude as mantle wall proportions change during ontogeny, with the relatively thin mantle walls of newly hatched squid experiencing significantly smaller differences in strain than the thicker mantle walls of adults. Second, we describe how the length–tension relationship of obliquely striated mantle muscles varies with position to accommodate the transmural gradient of strain, with the result that circular muscle fibers near the inner and outer surfaces of the mantle are predicted to produce similar force during mantle contraction. The factors that affect the length–tension relationship in obliquely striated muscles are unknown, and thus we have not yet identified the mechanism(s) responsible for the transmural shift in the length–tension properties of the mantle circular fibers. We have, however, developed a mathematical model that predicts small changes in the oblique striation angle (which varies from 4 to 12° in adult squid) have a significant effect on the shape of the length–tension relationship, with lower angles predicted to result in a broader length–tension curve.

Introduction

Length–tension relationships are fundamental to the functions of striated muscles and musculoskeletal systems. In the musculoskeletal systems of soft-bodied invertebrates, the absence of joints and tendons can result in extensive variation in muscle shortening and elongation during body movements (e.g., Lanzavecchia 1977; Gerry and Ellerby 2011; Thompson et al. 2014, 2016). An individual invertebrate muscle fiber may thus be required to produce force over an exceptionally broad range of operating lengths compared with a vertebrate striated fiber of similar length. In addition, the operating length range of an invertebrate muscle fiber appears to depend on the size, shape, and relative proportions of the animal (Thompson et al. 2010a). The length–tension relationships of soft-bodied invertebrate muscles may thus be molded, in part, by different constraints from the striated muscles of animals with jointed skeletal support systems.

In this paper, we highlight the importance of considering muscle function across spatial scales in soft-bodied invertebrates, especially the factors that affect the operating length ranges and length–tension relationships of the obliquely striated muscles that are common in these animals. First, we integrate our recently published work with the results of new experiments to investigate the ways in which body

Advance Access publication June 4, 2018

size and shape affect muscle operating length ranges in cephalopod molluscs. Second, we review recent work showing that the length–tension relationship and operating length range of squid mantle circular muscle vary as a function of position in the mantle wall. At the end of this review, we present a newly developed model that suggests a novel mechanism for adjusting the length–tension relationship of obliquely striated muscles.

Do body size and shape affect muscle operating length ranges in invertebrates?

Body shape and size pose unique challenges to striated muscle function in the musculoskeletal systems of soft-bodied invertebrates. Many of these animals have hollow, cylindrical bodies supported by hydrostatic skeletal support systems. The biomechanical principles guiding the function of hydrostatic skeletons have been described in detail previously (e.g., Kier and Smith 1985; Kier and Thompson 2003; Kier 2012). Briefly, the hydrostatic body wall is incompressible at physiological pressures. Since the body wall volume is thus essentially constant, changes in one dimension must be accompanied by compensatory changes in one or both of the other two dimensions.

We developed a mathematical model (Thompson et al. 2008, 2010a) of a soft-bodied animal with a hollow, cylindrical body shape. If the length of the body is assumed to be constant (an accurate assumption for the mantle of squids) and the "circular" muscle fibers (i.e., muscle fibers whose long axes are oriented circumferentially) of the body wall contract to decrease diameter, the thickness of the muscular body wall must increase (Fig. 1A). As body wall thickness increases, the model predicts that large non-uniformities in strain across the body wall must occur, such that the circular muscle fibers near the inner lumen surface of the body wall undergo greater shortening than fibers near the outer surface (Thompson et al. 2010a; Fig. 1A).

The predictions of the model lead to three hypotheses: (H1) a transmural gradient of circumferential strain exists across the body wall, with greater strain in the circular muscle fibers near the inner surface relative to the outer surface; (H2) the transmural gradient of strain increases as the amplitude of body contraction increases; and (H3) the transmural gradient of strain is greater for individuals with relatively thicker body walls.

Previous work provided support for the first two hypotheses in the mantle of adult squid, with

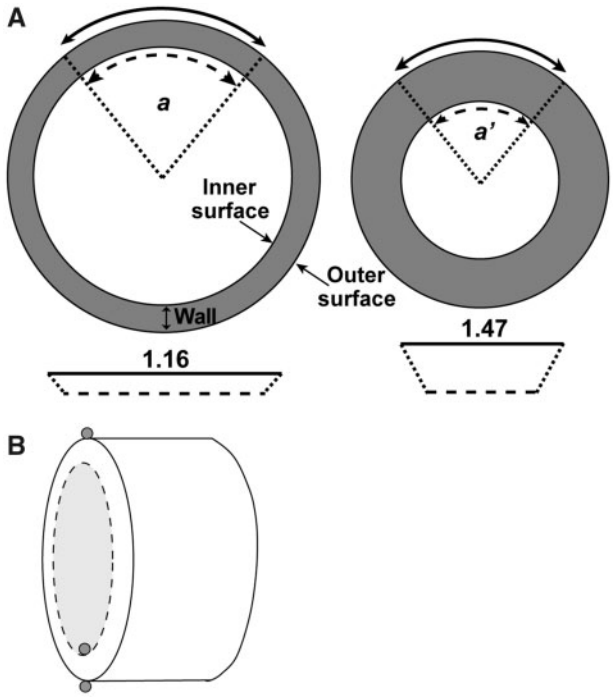

Fig. 1 (**A**) Schematic illustrating the relative lengths of the outer and inner surfaces of the mantle prior to contraction (*a*, ratio of outer:inner=1.16) and after a 30% decrease in the circumference of the outer surface (*a*′, ratio=1.47). The inner surface of the mantle experiences a proportionally greater change in length. (**B**) Mantle ring schematic to illustrate placement of the sonomicrometry transducers (gray filled circles). The dashed line marks the inner lumen surface of the mantle; the solid lines indicate the outer surface.

circular muscle fibers near the inner surface of the mantle experiencing circumferential strains 1.3 to 1.4-times greater than fibers near the outer surface of the mantle during the same contraction (Thompson et al. 2010a). In order to test all three hypotheses, we determined whether gradients of strain exist in squid (H1) and measured these gradients of strain for jets of different amplitudes (H2) and in animals of different life stages that experience an ontogenetic increase in the relative thickness of the mantle wall (H3).

Methods: Mantle diameter measurements in swimming squid

We measured changes in mantle diameter and wall thickness in juvenile and adult squid ($n=8$) using sonomicrometry as described in Thompson et al. (2010a). Because juveniles resemble adults in body shape and locomotor behaviors, we pooled their data and will refer to this group simply as "adults" for comparison with hatchlings. Briefly, adult *Doryteuthis pealeii* ($n=8$) were anesthetized in cold seawater (3–4°C Bower et al. 1999) while

sonomicrometry crystals were affixed surgically to the outer surface of the mantle with suture and to the inner lumen surface with 3M Vetbond (3M Animal Care Products, St. Paul, MN, USA). The transducers were attached along the dorsal and ventral midlines in a single transverse plane that was about one-third of the dorsal mantle length (DML) from the anterior edge of the mantle; their configuration permitted simultaneous measurements of mantle diameter and wall thickness (Fig. 1B).

Following surgery, squid were transferred to a shallow tank (2 ×1×0.15 m deep) filled with seawater at 15°C. We elicited swimming at various speeds while the sonomicrometer (Triton Technology, San Diego, CA, USA) simultaneously recorded changes in the diameter of the outer surface of the mantle and the accompanying changes in mantle wall thickness at 1000 Hz. The number and type of jets elicited from each animal are reported in Supplementary Table S1 (Supplementary Materials). At the end of the swimming trial, we euthanized each squid by over-anesthetizing it in aqueous magnesium chloride solution (Messenger et al. 1985). Post-mortem, we evaluated the alignment of the transducers, measured DML, and cut a cross-section of the mantle at one-third DML in order to measure resting diameter and wall thickness. We also measured resting diameter and wall thickness in other adult animals which led to a wall thickness: diameter sample size of $N=48$, including the eight animals used in the sonomicrometry measurements.

Because newly hatched *D. pealeii* are quite small (mean DML ≈ 1.8 mm), we developed other methods for measuring diameter and wall thickness. First, we measured mantle diameter in swimming hatchlings using videography. *Doryteuthis pealeii* hatchlings were placed in a tank (10 ×6×10 cm) filled with seawater at 17–20°C. We elicited a range of swimming speeds and recorded them using a pair of synchronized high-speed video cameras (125 frames/s; Troubleshooter, Fastec Imaging, San Diego, CA, USA). ImageJ software (Schneider et al. 2012) was used to digitize changes in mantle diameter during multiple jets ($n=85$ jets from $N=17$ individuals; more detail in Supplementary Table S1). Measurements were taken at the ink sac, which is located $^1/_3$–$^1/_2$ DML from the anterior edge of the mantle (Fig. 2A). The pixel resolution of the cameras limited us to a maximum spatial resolution in the field of view of the camera of ±0.0028 mm^2, which represents an error of ±0.28% for a mantle diameter of 1 mm, which is a typical diameter for *D. pealeii* hatchlings. Because diameter was used to calculate wall thickness, this error propagates as a ±5% error in the wall thickness calculation.

Mantle wall thickness of the hatchlings could not be measured directly from the video. Instead, in a separate analysis we found the morphological relationship between diameter and wall thickness and used it to estimate wall thicknesses for each observed diameter. To find the relationship between wall thickness and diameter, hatchlings ($n=19$) were fixed in 10% formalin in seawater for 96 h and stored in 70% aqueous ethyl alcohol. All the animals were euthanized by destroying the brain with a pin prior to fixation. Some animals were placed in an aqueous magnesium chloride solution (Messenger et al. 1985) to relax the musculature and expand the mantle radially prior to euthanasia and fixation. Other hatchlings were fixed immediately following euthanasia. This procedure allowed us to sample hatchlings over a range of mantle contraction.

Hatchlings were then rehydrated in three changes of artificial seawater. We measured DML before embedding the hatchlings in optimal cutting temperature compound (Tissue Tek OCT Compound, Sakura Finetek, Inc., Torrance, CA, USA). We cut 40 µm-thick sections at the location of the ink sac with a cryostat at −18°C (Fig. 2B). Circumference (C) and wall thickness were measured from photomicrographs using ImageJ software. Mantle diameter (D) was calculated from circumference ($D=C/\pi$). We found the relationship between diameter and wall thickness and used it to estimate wall thickness for a given diameter measured for a jet.

Methods: Calculation of circumferential strain

Using the model described by Thompson et al. (2008, 2010a), circumferential strain at the outer surface (ε_{out}) and the inner lumen surface (ε_{in}) of the mantle were defined as:

$$\varepsilon_{OUT} = \frac{(d_r - d_i)}{d_r}, \quad (1)$$

$$\varepsilon_{IN} = \frac{(d_r - 2t_r) - (d_i - 2t_i)}{d_r - 2t_r}, \quad (2)$$

where d_i and t_i are the instantaneous diameter of the outer surface of the mantle and wall thickness, respectively, measured during jetting, and d_r and t_r are the diameter and wall thickness of the mantle at rest. Since the mantle wall thickness could not be measured directly for the hatchlings from the video, wall thickness for a given observed mantle diameter was calculated from the linear relationship found between diameter and wall thickness (Fig. 2C), for the fixed squid as described above.

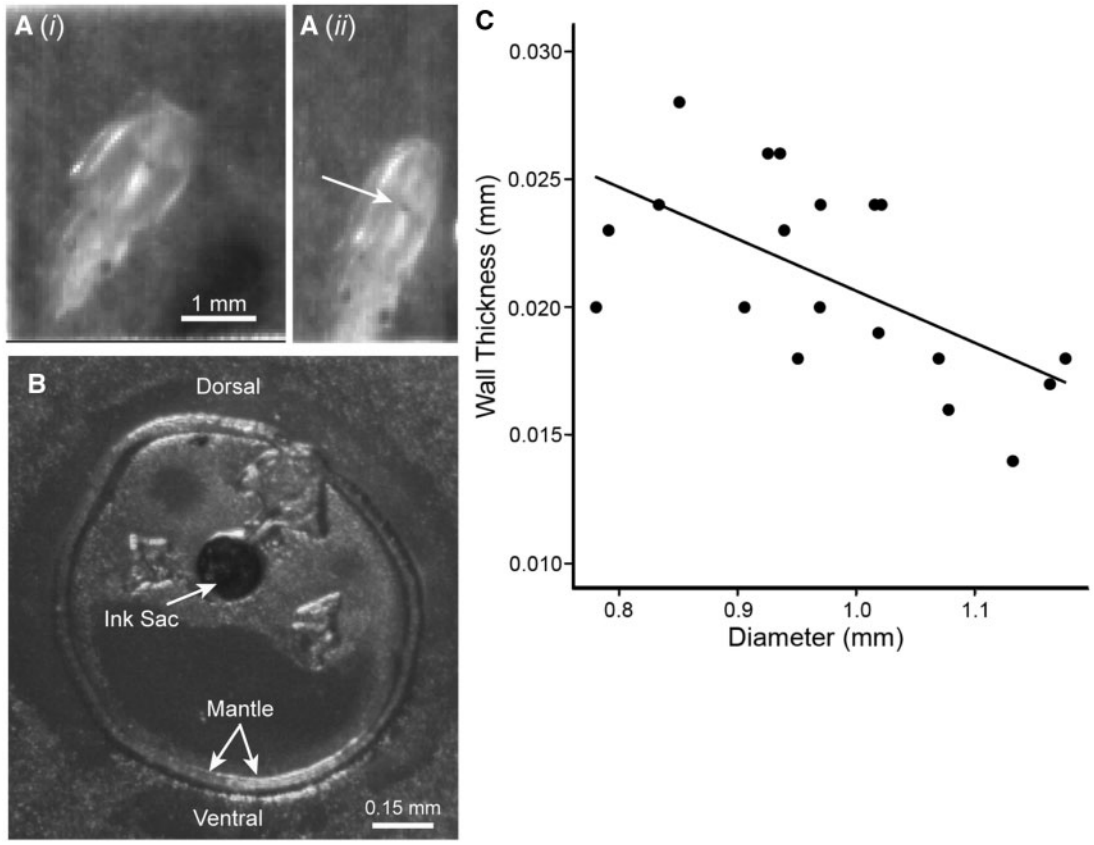

Fig. 2 Methods for measuring changes in mantle shape during swimming in *D. pealeii* hatchlings. (**A**) Video analysis of hatchling jetting recorded using high-speed video (125 frames/s). For a given jet, we measured diameter at the ink sac and found the maximum diameter prior to jetting (A, i) and the minimum diameter at the end of the jet (A, ii). Diameter was either measured laterally, as shown here, or dorso-ventrally, depending on the orientation of the hatchling relative to the camera. (**B**) Hatchling mantles were sectioned using a cryostat (40 μm-thick). We measured circumference and wall thickness in a section containing the ink sac. We used these measurements to find (**C**) the relationship between diameter and wall thickness ($n = 19$). The relationship measured here was $y = -0.02x + 0.041$. We then used the diameters measured from (A) and the relationship shown in (C) to calculate wall thickness during each jet and, subsequently, the strains experienced at the inner and outer surfaces of the hatchling mantle.

Methods: Statistical analysis

Statistical analyses were performed using R (v.2.15.2). Means are reported ±SD and were compared using *t*-tests. To test the first hypothesis, we calculated the mean difference in strain between the inner and outer surfaces of the mantle during jetting for each individual and then averaged individual means to determine the mean for each group. We fit linear models to the data, which included lifestage (i.e., hatchlings, adults), jet amplitude, and the interaction between jet amplitude and life stage as fixed effects. This produced linear relationships for each group and allowed for different slopes. These linear relationships were compared using analysis of covariance (ANCOVA). A *P*-value <0.05 was considered significant. For the hatchling wall thickness: diameter relationship, slope, and *y*-intercept are reported with 95% confidence intervals.

Results: Gradients of strain

The diameter and wall thickness measurements of the *D. pealeii* hatchlings fixed in formalin ($n = 19$) are displayed in Fig. 2C. The relationship between the wall thickness and diameter appeared to be linear for the available range of sizes. The best-fit line (slope: -0.020 ± 0.014, *y*-intercept: 0.041 ± 0.013 mm) had an R^2 of 0.37 and diameter explained a significant amount of the wall thickness variation ($P = 0.00536$).

During ontogeny (Fig. 3A), the thickness of the mantle wall increased with positive allometry relative to DML ($y = 0.000046x^{1.13}$, $R^2 = 0.975$; Fig. 3B, solid line), as indicated by an exponent >1 ($P < 0.001$; $N = 48$ adults and 17 hatchlings). The diameter of the mantle in anesthetized animals exhibited negative allometry relative to DML ($y = 0.44x^{0.72}$, $R^2 = 0.982$; Fig. 3B, solid line), as shown by an exponent <1

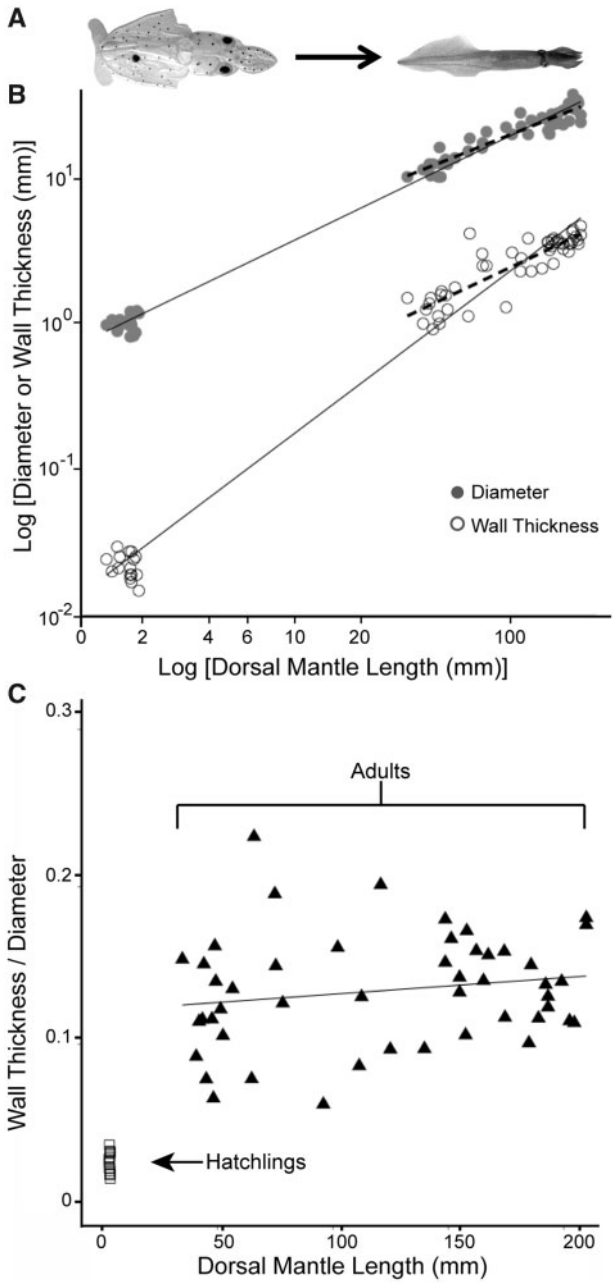

Fig. 3 The relationships between wall thickness, diameter, and dorsal mantle length (DML) in *D. pealeii* squid at different life history stages. (**A**) Photographs illustrating the relative change in body proportions between a hatchling (left side; DML = 1.8 mm) and an adult squid (DML=325 mm). (**B**) A log–log plot of diameter (filled symbols) and wall thickness (open symbols) against DML ($n = 19$ hatchlings; $n = 31$ juveniles and adults). For the full size range (solid lines), the relationship between diameter and DML showed negative allometry ($y = 0.44x^{0.72}$, $R^2 = 0.982$) while the relationship between wall thickness and DML exhibited positive allometry ($y = 0.000046x^{1.13}$, $R^2 = 0.975$). We interpret these relationships to mean that wall thickness increases faster than diameter during growth. Considering only the juveniles and adults (dashed lines), the fits (DML vs. diameter: $y = 1.71x^{0.596}$, $R^2 = 0.89$; DML vs. wall thickness: $y = 0.004x^{0.705}$, $R^2 = 0.76$) did not have significantly different exponents ($P = 0.107$). (**C**) The ratio of wall thickness to diameter (WT:D) vs. DML. Smaller animals (i.e., smaller DML) exhibited lower WT:D ratios than larger animals. The relationship between WT:D and DML was $y = 1.05 * 10^{-4}x + 0.12$ for adults and juveniles only ($n = 19$, indicated by the bracket). This slope was not significantly different from zero ($P = 0.17$). The relationship between WT:D and DML seemed to include a discontinuity between small and large squid, perhaps due to a quasi-metamorphosis between the hatchling and juvenile/adult stages. WT:D for hatchlings ($n = 31$; 0.022 ± 0.006) was significantly lower than for adults (0.128 ± 0.034; $P < 0.001$).

($P < 0.001$). Notably, when only juveniles and adults were considered, the exponents of both relationships were lower did not differ significantly ($P = 0.107$; DML vs. wall thickness: $y = 0.004x^{0.705}$, $R^2 = 0.76$; DML vs. diameter: $y = 1.71x^{0.596}$, $R^2 = 0.89$; Fig. 3B, dashed lines). Although the slope of the relationship between the ratio of mantle wall thickness:diameter (WT:D) and DML for adults and juveniles was positive ($y = 1.05 * 10^{-4}x + 0.12$), it was not significantly different from zero ($P = 0.17$, Fig. 3C). The average WT:D for hatchlings (0.022 ± 0.006) was, however, significantly lower than for adults (0.128 ± 0.034; $P < 0.001$), indicating that the relative thickness of the mantle wall increased over development. DML varied little among hatchlings. The disjointed nature of the relationship between DML and WT:D (Fig. 3C) is likely a reflection of a metamorphosis-like shape transition between hatchling and juvenile stages (Fig. 3A). Following "metamorphosis," growth occurs by increasing size without extensive shape change. Ontogenetic shape changes highlight the importance of considering body shape when analyzing muscle function during locomotion in soft-bodied invertebrates.

The circumferential strains measured for *D. pealeii* adults ($N = 8$, $n = 375$ jets) along the inner surface of the mantle ranged from −42% to +25% of resting circumference, where negative strains indicate contraction of the mantle and positive strains indicate hyperinflation, or an increase in mantle diameter from rest. *Doryteuthis pealeii* hatchlings ($N = 17$, $n = 85$ jets) experienced circumferential strains along the inner surface of the mantle ranging from −55% to +17% of resting circumference (Fig. 4A). Thus, some of the strains along the inner surface of the hatchling mantle were 1.3 to 1.4-times larger than those experienced by the adults. Hatchlings exhibited a striking absence of low strain jets, suggesting that low amplitude jetting is uncommon in this life stage.

We plotted inner and outer circumferential strains against outer strain. Strain at the outer surface served as a proxy of jet amplitude, with greater

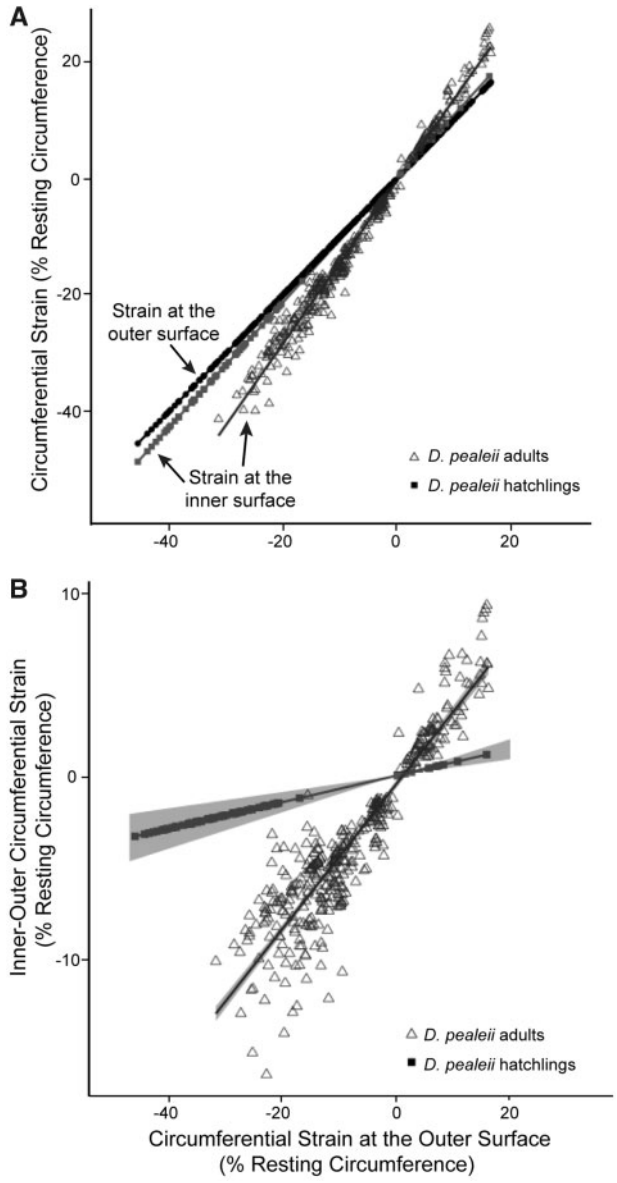

Fig. 4 Measures of strain (**A**) and gradients of strain (**B**) plotted against the circumferential strain at the outer surface of the mantle. Strain at the outer surface was used as a proxy for jet amplitude. (A) Circumferential strain along the inner and outer surfaces of the mantle. Negative strain values arbitrarily represent a decrease in mantle circumference, as occurs during the exhalant phase of the jet (adults $N = 8$, $n = 288$ jets; hatchlings $N = 17$, $n = 72$ jets). Positive values represent an increase in mantle circumference beyond the resting circumference, as occurs during hyperinflations of the mantle that often precede escape jets (adults $N = 7$, $n = 87$ jets; hatchlings $N = 4$, $n = 13$ jets). Best-fit lines for circumferential strain at the outer surface of the mantle (black line) for all jets ($y = x - 4.4 * 10^{-15}$, $R^2 = 1$) and circumferential strain at the inner surface for jets from each group (adults: $1.40x - 0.254$, $R^2 = 0.985$; hatchlings: $y = 1.07x - 0.19$, $R^2 = 1$) are shown. Best-fit lines for circumferential strains at the inner surface had significantly different slopes for each group of animals than for the circumferential strain at the outer surface (ANCOVA: $P < 0.001$). (B) The magnitude of the difference in circumferential strain between the inner and outer surfaces of the mantle (i.e., the transmural "gradient" of strain). Negative values represent mantle contractions; positive values represent hyperinflations of the mantle. The best-fit lines are shown for adults ($y = 0.4x - 0.25$) and hatchlings ($y = 0.07x - 0.19$). Slopes of the best-fit lines were significantly different in comparisons between adults and hatchlings (ANCOVA: $P < 0.001$). Note that the $R^2 = 1$ for the best fit line for circumferential strain at the outer surface (see panel A) because the "outer" strain values were plotted against themselves and therefore must yield a perfectly straight line. The $R^2 = 1$ for the inner circumferential strain for *D. pealeii* hatchlings (see A) and for the gradient of strain (see B) occurred because these values were calculated from a linear relationship between diameter and wall thickness and therefore must also have a perfect relationship. To account for the uncertainty in the relationship between wall thickness and diameter for hatchlings, we found the 95% confidence intervals for the slope of this relationship (Fig. 2C) and recalculated the gradient of strain at the upper and lower extremes for our estimate of slope. These results are shown as the shaded region behind the hatchling data. We also included the 95% confidence interval for the fit to the adult data for comparison (shaded region around adult fit).

strains indicating more vigorous jets (Fig. 4A). The best fit lines for outer circumferential strain and inner circumferential strain for each group are listed in Fig. 4A. The high R^2-value ($R^2 = 1$) of the outer circumferential strains was a consequence of plotting these values against themselves. The inner circumferential strains for the hatchlings also exhibit an R^2 of 1 because these strains were calculated using the linear relationship between diameter and wall thickness (Fig. 2C).

The mean gradient of strain (i.e., $\varepsilon_{in} - \varepsilon_{out}$; Equations (1) and (2)) during mantle contraction was significantly different from zero (*t*-test, $P < 0.001$) for *D. pealeii* adults ($-5.4 \pm 1.5\%$ resting circumference) and *D. pealeii* hatchlings ($-2.2 \pm 0.4\%$ resting circumference). The relationship between the magnitude of gradients of strain and jet size exhibited slopes that were significantly different from zero for each group ($P < 0.001$; see Fig. 4B for equations). In addition, the relationships were significantly different between adults and hatchlings (ANCOVA; $P < 0.001$). Because we used a single linear relationship (Fig. 2C) to calculate inner strain from the hatchling diameter data, however, the gradients of strain for hatchlings do not reflect uncertainty about the relationship between wall thickness and diameter. To account for this uncertainty, we found the 95% confidence interval of the slope of the relationship between wall thickness and diameter (Fig. 2C) and recalculated the gradients of strain using the extremes of this confidence interval. We plotted these findings as a region of uncertainty around the hatchling data as well as the 95%

confidence intervals for the fit for the adult data (Fig. 4B). These two regions do not overlap, suggesting that the differences observed between hatchlings and adults are real.

Discussion: Gradients of strain

The measurements of mantle circumferential strain supported the hypothesis that a transmural gradient of strain exists in the mantle (H1). Hatchlings experienced larger strains near the inner surface than near the outer surface (Fig. 4) as predicted, consistent with the trends observed for adult *D. pealeii* and *Sepioteuthis lessoniana* by Thompson et al. (2010a). Thus, we have demonstrated that gradients of strain exist across life stages within *D. pealeii*, confirming the importance of these gradients in loliginid squids and suggesting broader applicability to diverse invertebrates with hollow, cylindrical bodies.

We also found evidence that the transmural gradient of strain increased with jet amplitude (H2). We used the strain near the outer surface of the mantle as a proxy for jet amplitude (e.g., greater strains indicated more vigorous jets) and plotted the gradient of strain against it (Fig. 4B). Because the slope was significantly different from zero, as jet size increased, the size of the gradient of strain also increased.

Finally, we found that transmural gradients of strain varied with body proportions (H3). Because adults and juveniles had greaterer ratios of wall thickness:diameter than hatchlings (Fig. 3C) and because they exhibited significantly different relationships between the gradient of strain and jet size (Fig. 4B), our results indicate that as the relative thickness of the mantle wall increased, the gradient of strain also increased.

Thus, at the spatial scale of a whole animal, body shape, and size have the potential to affect the operating length ranges of the muscles that provide power for locomotion and movement.

Does the length–tension relationship of mantle muscles change transmurally?

One consequence of a transmural gradient of strain is that during mantle contraction and expansion the circular muscle fibers near the inner surface of the mantle may experience significantly greater excursions than circular fibers near the outer surface. This could result in fibers near the inner surface spending a smaller fraction of the contraction cycle in the maximum force region of the length–tension curve. Submaximal force production is potentially problematic for muscles whose primary role is providing power for jet thrust, especially since they lack obvious mechanisms of power amplification (e.g., joints and tendons). The gradient of strain could also result in circular fibers from different regions of the mantle wall producing different forces at a given instant in the contraction cycle, thus potentially reducing the maximum power output of mantle contractions, especially during escape jet locomotion. These transmural differences in excursion could be mitigated by adjusting the length–tension relationship of the circular fibers as a function of position in the mantle wall, so that all of the circular fibers produce similar forces at any point in the cycle.

Thompson et al. (2014) hypothesized that the circular muscle fibers from the inner surface produce higher forces, relative to the maximum isometric force (P_0), on the ascending and descending limbs of the length–tension curve than fibers from near the outer surface. In other words, they predicted that the length–tension curve for the circular fibers from near the inner surface would have ascending and descending limbs with shallower slopes than length–tension curves for fibers from near the outer surface. This hypothesis assumed that all of the circular muscle fibers in the mantle operate on roughly similar regions of the length–tension curve during the mantle contraction cycle (i.e., there is no transmural staggering of resting sarcomere lengths). Thus, testing the hypothesis required experiments in which the length–tension relationship could be compared with the *in vivo* muscle operating length range.

Soft-bodied invertebrates typically lack landmarks that can be used to relate muscle length changes to body or appendage kinematics. Furthermore, the curved shapes of many invertebrate muscular organs make it difficult to measure muscle operating length ranges using sonomicrometry. Testing the hypothesis required a method to overcome these difficuluties (see Thompson et al. [2014] for details). Briefly, sonomicrometry (methods as described in the previous section) was used to measure mantle circumference kinematics during jet locomotion in 10 adult *D. pealeii*. A full repertoire of jetting behavior was recorded in a large swim tunnel for each animal. The animals were then anesthetized in cold (3°C) seawater and euthanized by decapitation. A ring of mantle tissue that included the sonomicrometry transducers (see Fig. 1B for the layout of the transducers) was removed, two reference marks were made on the ring using a surgical marking pen, and the ring was photographed. The ring was then slit at the dorsal midline, "unfurled," and the inner or outer surface of the mantle glued to the temperature-controlled stage of a vibratome. A fine

insect pin was used to perforate the mantle where the two reference marks were located, the mantle tissue was photographed again, and then thin (300 μm) sheets of muscle tissue were sliced from the outer and inner surfaces by the vibratome. Each sheet was dissected into a small circular muscle preparation that included the pin holes.

The fibers near the inner surface of the mantle were lengthened slightly while those near the outer surface were shortened slightly as the cylindrical mantle sections were unfurled for vibratome sectioning. The effect of any differential fiber strain due to the alteration of mantle geometry (i.e., circular to flat shape) associated with the tissue preparation was likely minimal because the strains were small compared with those experienced *in vivo* (Thompson et al. 2014).

The length–tension relationship for each preparation was determined using a single stimulus pulse (2 ms pulse width, 1 Hz). The preparation was shortened to 0.8-times the length that provided maximum isometric twitch force, and then the length–tension relationship determined using tetanic stimulation (2 ms pulse width, 80 Hz, 100 ms duration). In all experiments, the current that elicited the maximum isometric force was used to stimulate the preparation.

In *D. pealeii*, both the length–twitch tension and length–tetanic tension relationships of the obliquely striated circular muscle fibers varied transmurally in the mantle wall. The circular fibers near the inner surface of the mantle produced higher force, relative to P_0, than circular fibers near the outer surface of the mantle at all points along the ascending limb of the length–tension curve (Thompson et al. 2014; Fig. 5). The mean maximum isometric tetanic stresses at L_0 (the preparation length that produced the maximum isometric tetanic force) for the fibers from the outer and inner surfaces of the mantle, respectively, did not differ significantly, suggesting that neither changes in myofilament length nor expression of different isoforms of myofilament proteins were responsible for the transmural difference in the length–tension relationship (Thompson et al. 2014; see Shaffer and Kier 2012). Moreover, the similarity in maximum isometric tetanic stress suggests that sarcomere lengths did not vary transmurally, as any changes in sarcomere length would require a change in thick filament length and, concomitantly, a change in maximum isometric force production (Josephson 1975).

The sonomicrometry experiments revealed that the circular muscle fibers operated *in vivo* primarily along the ascending limb of the length–tension curve. The fibers functioned routinely over muscle lengths at which force output ranged from only 85% to 40% of P_0, and during escape jets from 100% to 30% of P_0 (Fig. 5). Indeed, the circular fibers were extended to lengths greater than L_0 only during hyperinflation of the mantle immediately preceding an escape jet (Thompson et al. 2014). Consistent with the data presented above, the circular muscle fibers near the inner surface of the mantle experienced a significantly greater operating length range for a given mantle contraction than fibers near the outer surface (Thompson et al. 2014; Fig. 5). Interestingly, mapping the *in vivo* muscle operating length ranges onto the length–tension curves showed that the difference in the length–tension relationship of the circular muscle fibers near the inner surface of the mantle was sufficient to allow all of the circular fibers in the mantle wall to produce approximately the same force at any stage of mantle contraction (Thompson et al. 2014).

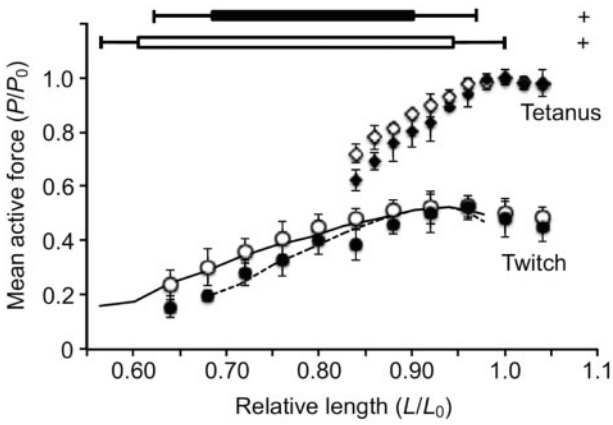

Fig. 5 The length–tension relationship and *in vivo* operating length ranges of the circular muscle fibers from near the outer (filled) and inner (open) surfaces of the mantle. The length–tension curves for muscle preparations for a twitch-style stimulus (single pulse; 2 ms pulse width) and a tetanic stimulus (2 ms pulses, 80 Hz, 100 ms duration) are shown. The solid (inner preparations) and dashed (outer preparations) lines represent the means of length–twitch force data. Linear regressions were fit to the length–tetanic force data for each squid for the data at lengths $\leq$0.95 L_0. The slopes of the ascending limbs differed significantly between the inner and outer preparations (independent samples *t*-tests: $t = 2.91$; $P = 0.017$), as did the *Y*-intercepts ($t = -2.40$; $P = 0.04$). The boxes above the length–tension curves show the *in vivo* operating length ranges of the circular fibers. The right edge of each box shows the mean muscle length (relative to L_{TW}) in the fully expanded mantle just prior to the start of mantle contraction, while the left edge shows the mean muscle length at the end of mantle contraction. The whiskers encompass 75% of the data that fell above the mean (right for mantle expansion) or below it (left for mantle contraction). The + symbols represent the largest hyperinflations from each group. Box plot sample size: 111 escape jets from each group.

Although the experiments supported the hypothesis proposed by Thompson et al. (2014), the mechanisms responsible for the observed transmural difference in length–tension properties are unknown. Studies of cross-striated muscle fibers have demonstrated that activation can affect the slope of the ascending limb of the length–tension curve (e.g., Rack and Westbury 1969; Chapple 1983), with greater activation leading to an increase in the slope of the ascending limb. Activation differences cannot explain the different length–tension relationships of the mantle circular muscles because a stimulation current that elicited the maximum force was used for all preparations (Thompson et al. 2014). Surprisingly, and contrary to the patterns observed in vertebrate striated muscle (Rack and Westbury 1969), all the mantle circular fibers produced maximum isometric twitch force at a shorter length (L_{TW}) than the length (L_0) of maximum isometric tetanic force, with no significant differences between the inner and outer preparations (Thompson et al. 2014; Fig. 6). For all preparations, L_{TW} was 6.1 ± 4.3% (mean ±SD) shorter than L_0 (Fig. 6B). Moreover, although the time required to achieve maximum isometric force and the 50% relaxation time both increased slightly as muscle preparation length increased, there were no significant differences in length-dependent contraction kinetics between the "inner" or "outer" muscle fibers (Thompson et al. 2014). We have not yet identified the mechanism(s) underlying the rightward shift of L_0 compared with L_{TW}, but this is an active area of investigation in our labs. Nevertheless, the transmural changes in length–tension behavior are not an artifact of the experimental approach but instead reflect inherent differences in the circular fibers themselves.

Ultrastructural differences between the circular muscle fibers from near the inner and outer surfaces of the mantle might explain the ability of the inner fibers to produce higher relative force along the ascending and descending limbs of the length–tension curve. In many striated muscles, longer thin and thick filaments and higher thin:thick filament ratios are correlated with higher force output (Jahromi and Atwood 1969; Josephson 1975; Granzier et al. 1991). Previous ultrastructural investigations of the circular mantle muscles of squids (Ward and Wainwright 1972; Moon and Hulbert 1975; Bone et al. 1981; Thompson and Kier 2006; Thompson et al. 2008, 2010b) did not report transmural differences in myofilament dimensions or their arrangement, but this has not been explored in a systematic way.

Intrinsic differences in the mantle circular muscle fibers might explain the transmural variation in length–tension properties. For example, protein kinase A-induced phosphorylation of two myofilament lattice proteins (troponin I and myosin binding protein C) in the cardiac myocytes of rats alters the shape of the length–tension curve, increasing the slope of the ascending limb dramatically (Hanft and McDonald 2010). Expression of different

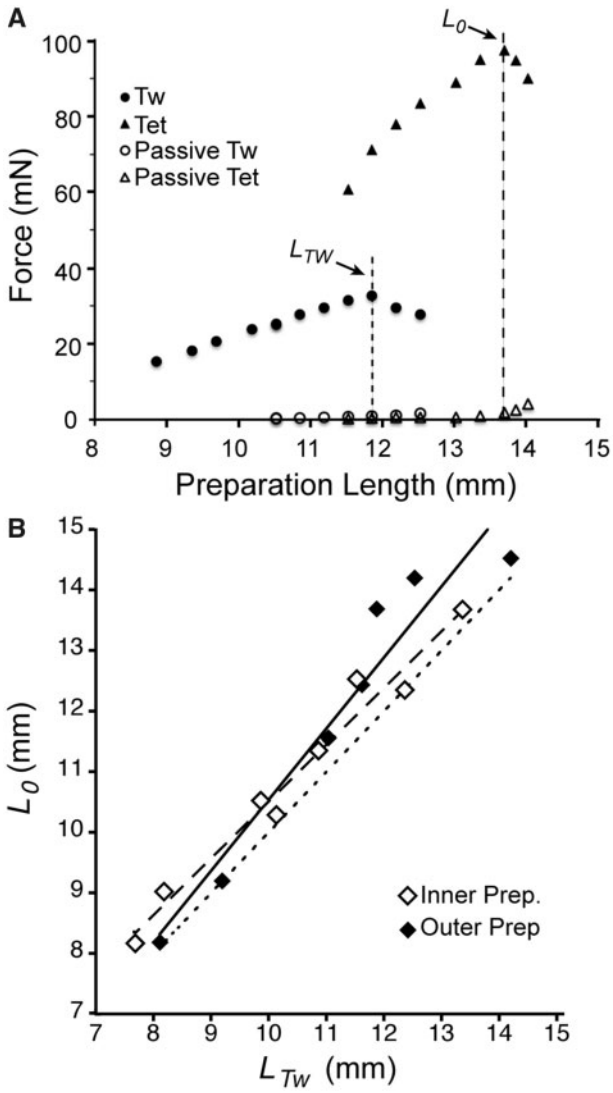

Fig. 6 Effect of stimulus frequency on the length–tension relationship. (**A**) Differences in the active and passive length–tension curves for a twitch-style stimulus (Tw; single pulse, 2 ms pulse width) and a tetanic (Tet; 2 ms pulses, 80 Hz, 100 ms duration) stimulus for a single muscle preparation. (**B**) The length (L_0) that produced maximum isometric tetanic force vs. the length (L_{TW}) that produced the maximum isometric twitch force. Each point represents data from a single preparation. The dotted line intersects the origin and has a slope of 1.0; the solid and dashed lines show linear regressions for the outer and inner muscle preparations, respectively. Inner preparations (open symbols): $Y = 0.94X + 1.16$, $R^2 = 0.97$, $F = 210$, $P < 0.001$, $n = 7$; outer preparations (filled symbols): $Y = 1.17X - 1.19$, $R^2 = 0.92$, $F = 68.5$, $P < 0.001$, $n = 6$.

troponin isoforms can also affect force production in cardiac fibers (Gordon et al. 2000). Additionally, recent work has revealed that the length–tension relationship depends on the radial distance between the thin and thick myofilaments (Williams et al. 2013). The potential role of such mechanisms in obliquely striated squid mantle muscle is unknown.

Although differences in myofilament lattice proteins have the potential to affect the length–tension relationship (e.g., Hanft and McDonald 2010) and additional research on this is needed, squid muscles modulate isometric force and shortening velocity by varying myofilament length, not by expressing different isoforms of myosin heavy chain (Kier and Schachat 1992, 2008; Kier and Curtin 2002; Thompson et al. 2010b; Shaffer and Kier 2012, 2016; Kier 2016). We are currently investigating the implications of differences in the dimensions and arrangement of myofilaments in our search for the mechanism driving transmural differences in muscle mechanics.

One possible mechanism for altering the length–tension relationship is unique to obliquely striated muscle and is a function of the arrangement of the myofilaments. Obliquely striated muscles, so-called because the dense bodies (i.e., *Z*-elements) are aligned at an oblique angle to the long axis of the cell (Fig. 7), have been reported in members of 17 invertebrate phyla (see list in Supplementary Materials). Obliquely striated fibers are ubiquitous in some (e.g., Nematoda), but are restricted in their distribution in others (e.g., the Mollusca, Urochordata, and Sipunculida). A detailed analysis of the evolution of these muscles is needed, but mapping the distribution onto a recent eumetazoan phylogeny (Paps et al. 2009) suggests that oblique striation evolved independently several times, presumably from a non-striated precursor (Prosser 1979, 1982).

Obliquely striated muscles differ structurally in several ways from cross-striated muscles. The thick and thin myofilaments of obliquely striated muscle, although parallel to the longitudinal axis of the fiber, are not aligned in register across the cell as in cross-striated fibers. Instead, the myofilaments are staggered in an oblique pattern (Fig. 7). In addition, obliquely striated muscle lacks transverse banding and a distinct *Z*-disc is absent. The thin myofilaments instead are anchored to rows of dense bodies (called *Z*-elements or *Z*-bodies; Fig. 7B), which are aligned at a low angle with respect to the longitudinal axis of the fiber. This angle, termed the striation angle (θ in Fig. 7A), increases as the fiber shortens and decreases as the fiber is elongated (Hanson and Lowy 1957). In addition to differences in the myofilament arrangement compared with cross-striated muscle, there are other differences in the myofilament dimensions, excitation–contraction coupling system, fiber size, and mitochondrial distribution (Rosenbluth 1972; Lanzavecchia 1977; Kier 1985, 1996).

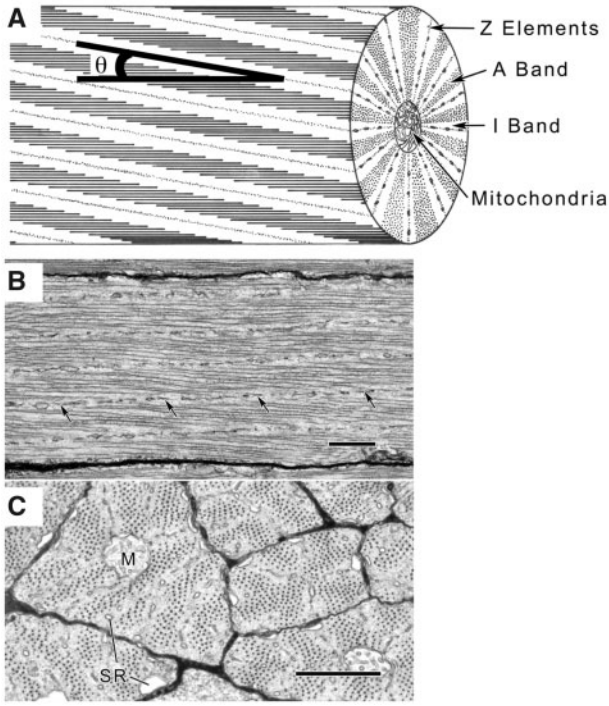

Fig. 7 (**A**) Diagram of an obliquely striated muscle fiber from a squid. Myofilaments surround a central core of mitochondria. The thick myofilaments (dark gray lines) are aligned parallel to the long axis of the cell but are not in register across the cell, thus forming a staggered array. Striation angle (θ) varies as the fiber shortens or is lengthened. Thin filaments are not illustrated (adapted from Kier, 1985). (**B** and **C**) Transmission electron micrographs of obliquely striated muscle fibers of the transverse muscle of the arms of loliginid squid in longitudinal section (B) and in transverse section (C). The longitudinal axis of the muscle fiber in B is oriented horizontally on the page. A row of *Z*-bodies (arrows) is oriented at a small oblique angle with respect to the horizontally oriented thick filaments. M, mitochondria; SR, sarcoplasmic reticulum. Scale bars=1 μm. Adapted from Kier and Curtin (2002) and Kier (1996).

Oblique striation is hypothesized to allow striated muscle to operate over an extreme range of muscle lengths, much greater than could be accommodated by cross-striated fibers (Rosenbluth 1965, 1972; Lanzavecchia 1977; Lanzavecchia and Arcidiacono 1981). Rigorous testing of this hypothesis has not occurred because there are few published accounts of the contractile properties of obliquely striated muscles. Although the obliquely striated longitudinal body wall fibers of the medicinal leech, *Hirudo*

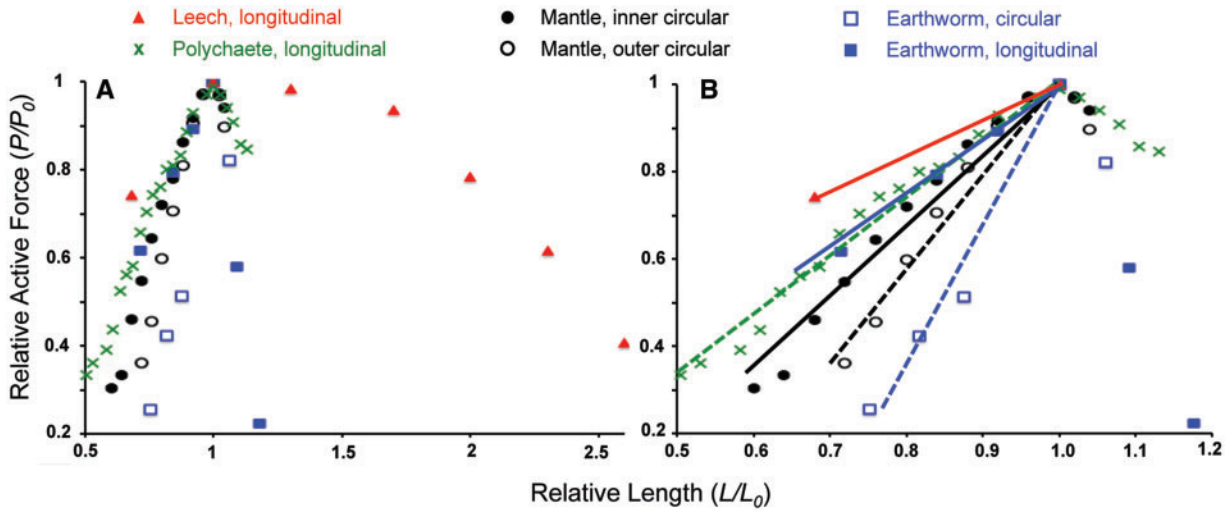

Fig. 8 (**A**) Length–tension curves for leech (*Hirudo verbana*; Gerry and Ellerby 2011), squid (*D. pealeii*; Thompson et al. 2014), polychaete (*Alitta virens*; Thompson, unpublished data), and earthworm (*Pheretima communissima*; Hidaka et al. 1969). (**B**) A magnified view of the ascending limbs of the curves. Note differences among species, between different muscles in one species of earthworm, and between circular muscle fibers from different regions of the same muscular organ in squid.

verbana, can produce relatively high force over an extraordinary range of muscle lengths, obliquely striated muscles are not universally capable of producing force over extreme muscle excursions (Fig. 8). Indeed, there appears to be extensive variation in the length–tension relationship among obliquely striated muscles, even among muscles from the same animal (Fig. 8B).

If the length–tension relationship of the obliquely striated mantle circular muscles can be adjusted in response to transmural gradients of strain, what mechanisms permit such adjustments? A recent geometrical model suggests that the properties of the length–tension relationship of an obliquely striated muscle depend on the resting myofilament striation angle (Olszewski-Jubelier 2015). In addition to the well-established effect on force of changes in overlap between the thick and thin myofilaments (Gordon et al. 1966) there is an additional effect in obliquely striated muscle because the striation angle, and thus the amount of stagger between adjacent myofilaments, changes as the muscle elongates and shortens (Fig. 9A, B). This change in stagger between adjacent filaments is referred to as "shearing." Although shearing in obliquely striated muscle was interpreted initially to be a separate and supplemental mechanism responsible for fiber shortening (Rosenbluth 1967), it was recognized later that changes in the striation angle are due simply to the geometry of an essentially constant volume fiber (Lanzavecchia 1977).

The geometrical model (see Supplementary Materials for details) calculates the amount of force produced by a single sarcomere based on the overlap of the myofilaments, taking into account the effect of sarcomere length on the striation angle and thus stagger between myofilaments (Olszewski-Jubelier 2015). Briefly, the following are prescribed initially: thick filament length, the length of two thin filaments plus the width of a dense body, the bare zone length, myosin head spacing, number of thick and thin filament pairs, and the striation angle (Fig. 9A, B). The model is constructed in two dimensions and holds sarcomere area constant to take into account the essentially constant volume of a muscle fiber, and to allow calculation of the striation angle as a function of changes in length. It thus does not consider the implications of the three-dimensional geometry of the various components of the fiber. The length is changed incrementally and the force calculated at each length based on the total number of cross-bridges with an adjacent thin filament available for interaction. As in empirical experiments, the force at each length is divided by the maximum isometric force (P_0) produced and the length is divided by the length at maximum force (L_0). The model allows exploration of the effects on the length–tension behavior of the initial striation angle, whether or not striation angle changes, and the lengths and spacing of the myofilaments. Although some of the input parameters of the model such as myofilament lengths and filament spacing are known for *Hirudo medicinalis* (Lanzavecchia et al. 1985), most are unknown (not just for *H. medicinalis* but for most species) and thus it is not possible at this point to predict the length–tension

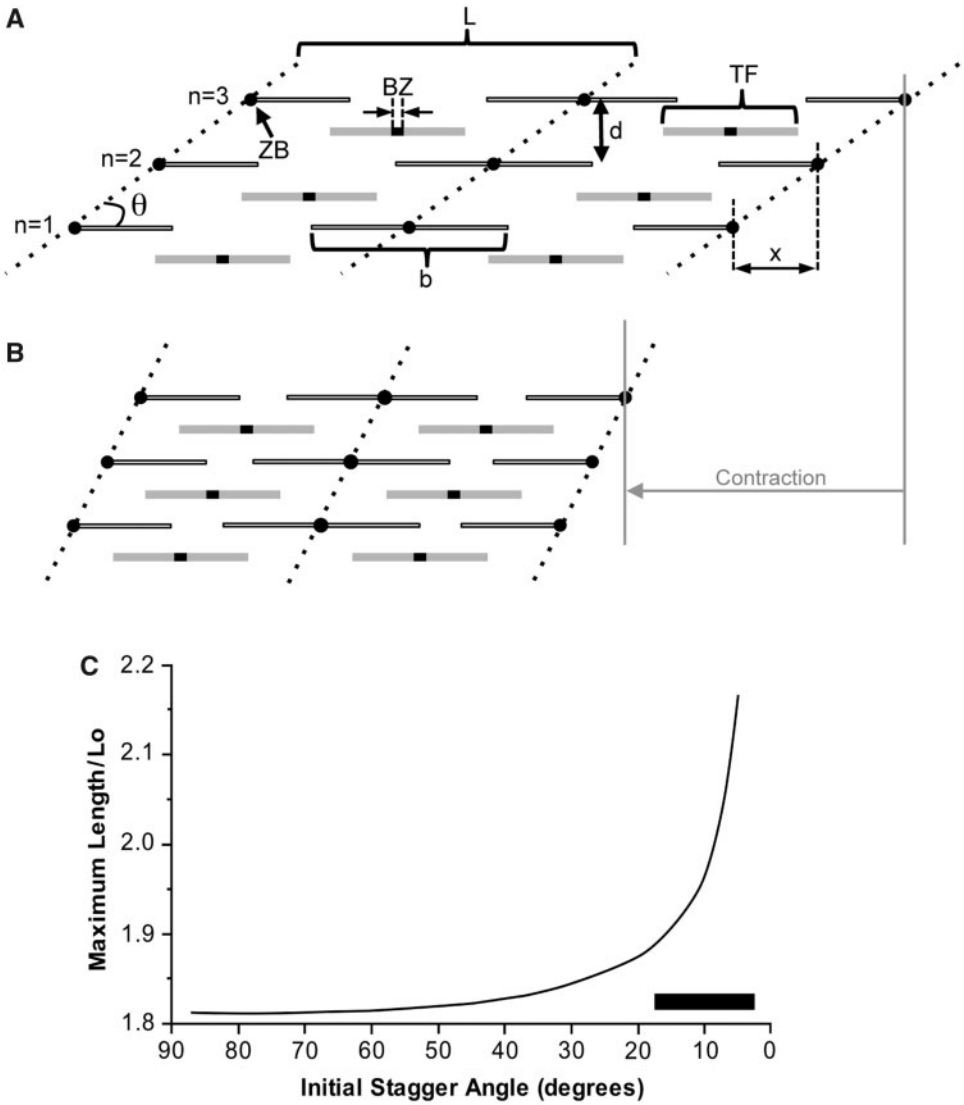

Fig. 9 (**A**) Obliquely-striated sarcomeres with dimensions considered in the model. L, the length of the sarcomere; b, the length of two thin filaments and one Z-body (ZB); x, the horizontal distance between two vertically adjacent thin filaments; d, distance between two thin filaments; n, number of filament pairs; BZ, the length of the bare zone; TF, the length of a thick filament; θ, angle of striation. The angle of striation is much greater than it would be *in vivo* for ease of illustration. See the Supplementary Materials section for details of the model. (**B**) The model sarcomere after a moderate amount of contraction to illustrate the increase in angle of striation (i.e., shearing of the thick filaments). The vertical gray lines indicate the amount of shortening that has occurred. (**C**) Predicted changes in the length–tension relationship with changes in striation angle. Maximum Length/L_0 corresponds to the *X*-intercept of the descending limb; higher values indicate a broader length–tension curve. Initial striation angle is measured at L_0 (fiber length at which maximum isometric force occurs). The black bar represents range of striation angles reported in the literature (Hanson and Lowy 1957; Rosenbluth 1965; Millman 1967; Thompson et al. 2010b) but with the exception of the data from Thompson et al. (2010b), it is unknown if reported values represent striation angle at L_0. Note that the *X*-axis is reversed (i.e., 0 is at the far right).

behavior for specific muscles. The model does provide, however, insight into the factors that have the greatest impact on the length–tension behavior.

One of the most interesting results of the geometrical model is that the initial striation angle has a large effect on the length–tension relationship. In particular, the smaller the initial striation angle, the greater the maximum relative length at which the muscle can produce force (Fig. 9C). This is ultimately an effect of the greater change in stagger between myofilaments, for a given change in overlap, that occurs at low striation angles. This is an exciting result because it provides a potential mechanism for adjustment of the body wall musculature of a soft-bodied invertebrate to match the range of muscle excursions they experience. More research is needed, however, since at this point we do not know if striation angles vary widely among different obliquely

striated muscles. In the mantle and funnel retractor muscles of squid, the striation angle at rest has been reported as ranging from 4° to 12° (Hanson and Lowy 1957), which is of interest since this includes the range of striation angles that have a large effect on the maximum length of the fibers (Fig. 9C), but we do not know the striation angles at L_0. Measurements on the mantle circular muscles of newly hatched and adult Atlantic longfin squid (*D. pealeii*) suggest that striation angle decreases significantly during ontogeny (i.e., from a mean of 22.8° to 4.6° with the muscles at L_0; Thompson et al. 2010b). An important first step in this research is to determine if striation angles at L_0 of the circular fibers decrease transmurally from the outer to the inner surfaces of the mantle in *D. pealeii*.

Discussion

We have shown that body size and shape can affect the operating length ranges of muscles. These effects are not limited to the mantle of squids; transmural gradients of strain may also affect other hollow, cylindrical structures, including the bodies and muscular organs of myriad soft-bodied invertebrates, arteries (Lillie and Gosline 2006), and muscle sphincters (Heldoorn et al. 2001). Furthermore, gradients of strain may affect connective tissues in addition to muscles (Kurth et al. 2014). In the thoracic aorta of pigs, for example, the elastic lamellae near the inner surface of the arterial wall are more highly crimped, and thus relatively longer, than those near the outer surface. This arrangement may help equalize strain in the lamellae despite the non-uniform circumferential strain that occurs as the aorta expands in diameter (Lillie and Gosline 2006). In addition, the orientation of collagen fibers varies transmurally in human brain arteries in response to non-uniform distribution of stress in the vessel wall (Finlay et al. 1995; Driessen et al. 2004).

Transmural gradients of strain also have implications for function at finer spatial scales than a body or organ. Individual circular muscle fibers experience very different operating length ranges depending on their position within the body wall and, at least in adult *D. pealeii*, the transmural gradient of strain is associated with a significant difference in length–tension relationship across the mantle wall. We speculate that transmural variation in length–tension relationships may be a common response to gradients of strain among soft-bodied invertebrates.

The magnitude of the gradient of strain increases substantially as the mantle wall thickens during ontogeny, suggesting that the length–tension relationship of an individual circular fiber may change during ontogeny as its relative position in the mantle wall changes. The mantle wall increases in thickness during growth due to both hypertrophy of existing fibers and hyperplasia of circular fibers (Moltschaniwskyj 1994). We do not know how the length–tension relationships of the newly formed fibers are determined, what mechanisms are used to adjust the length–tension relationships of existing or newly formed fibers, or the extent to which those mechanisms are shared among obliquely striated muscles from diverse taxa. These represent exciting areas of research that have the potential to reveal new fundamental principles of striated muscle function.

Acknowledgments

We thank Drs. N. Holt and D. Williams for organizing the symposium and inviting us to participate. We also thank Dr. N. Konow and three anonymous reviewers for helpful suggestions on a previous version of this manuscript. We thank S. Whitfield for assistance with the graphics and Dr. T.L. Hedrick for advice on MATLAB.

Funding

This work was supported by the National Science Foundation (grants IOS-1557838 and IOS-0950827) and the Committee on Grants at Franklin & Marshall College.

Supplementary data

Supplementary data available at *ICB* online.

References

Bone Q, Pulsford A, Chubb AD. 1981. Squid mantle muscle. J Mar Biol Assoc U.K. 61:327–42.

Bower JR, Sakurai Y, Yamamoto J, Ishii H. 1999. Transport of the ommastrephid squid *Todarodes pacificus* under cold-water anesthesia. Aquaculture 170:127–30.

Chapple WD. 1983. Mechanical responses of a crustacean slow muscle. J Exp Biol 107:367–83.

Driessen JB, Wilson W, Bouten CVC, Baaijens FPT. 2004. A computational model for collagen fibre re-modelling in the arterial wall. J Theor Biol 226:53–64.

Finlay HM, McCullough L, Canham PB. 1995. Three-dimensional collagen organization of human brain arteries at different transmural pressures. J Vasc Res 32:301–12.

Gerry SP, Ellerby DJ. 2011. Serotonin modulates muscle function in the medicinal leech *Hirudo verbana*. Biol Lett 7:885–8.

Gordon AM, Huxley AF, Julian FJ. 1966. The variation in isometric tension with sarcomere length in vertebrate muscle fibres. J Physiol 184:170–92.

Gordon AM, Homsher E, Regnier M. 2000. Regulation of contraction in striated muscle. Physiol Rev 80:853–924.

Granzier HL, Akster HA, Ter Keurs HE. 1991. Effect of thin filament length on the force–sarcomere length relation of skeletal muscle. Am J Cell Physiol 260:C1060–70.

Hanft LM, McDonald KS. 2010. Length dependence of force generation exhibit similarities between rat cardiac myocytes and skeletal muscle fibres. J Physiol 588:2891–903.

Hanson J, Lowy J. 1957. Structure of smooth muscles. Nature 180:906–9.

Heldoorn M, van Leeuwen JL, Vanderschoot J. 2001. Modelling the biomechanics and control of sphincters. J Exp Biol 204:4013–22.

Hidaka T, Kuriyama H, Yamamoto T. 1969. The mechanical properties of the longitudinal muscle in the earthworm. J Exp Biol 50:431–43.

Jahromi SS, Atwood HL. 1969. Correlation of structure, speed of contraction, and total tension in fast and slow abdominal muscle fibers of the lobster (*Homarus americanus*). J Exp Zool 171:25–37.

Josephson RK. 1975. Extensive and intensive factors determining the performance of striated muscle. J Exp Zool 194:135–54.

Kier WM. 1985. The musculature of squid arms and tentacles: ultrastructural evidence for functional differences. J Morphol 185:223–39.

Kier WM. 1996. Muscle development in squid: ultrastructural differentiation of a specialized muscle fiber type. J Morphol 229:271–88.

Kier WM. 2012. The diversity of hydrostatic skeletons. J Exp Biol 215:1247–57.

Kier WM. 2016. The musculature of coleoid cephalopod arms and tentacles. Front Cell Dev Biol 4:10.

Kier WM, Smith KK. 1985. Tongues, tentacles and trunks: the biomechanics of movement in muscular-hydrostats. Zool J Linn Soc 83:307–24.

Kier WM, Schachat FH. 1992. Biochemical comparison of fast- and slow-contracting squid muscle. J Exp Biol 168:41–56.

Kier WM, Curtin NA. 2002. Fast muscle in squid (*Loligo pealei*): contractile properties of a specialized muscle fibre type. J Exp Biol 205:1907–16.

Kier WM, Schachat FH. 2008. Muscle specialization in the squid motor system. J Exp Biol 211:164–9.

Kier WM, Thompson JT. 2003. Muscle arrangement, function and specialization in recent coleoids. Berl Paläobiol Abh 03:141–62.

Kurth JA, Thompson JT, Kier WM. 2014. Connective tissue in squid mantle is arranged to accommodate strain gradients. Biol Bull 227:1–6.

Lanzavecchia G. 1977. Morphological modulations in helical muscles (Aschelminthes and Annelida). Int Rev Cytol 51:133–86.

Lanzavecchia G, de Eguileor M, Valvassori R. 1985. Superelongation in helical muscles of leeches. J Muscle Res Cell Motil 6:569–84.

Lanzavecchia G, Arcidiacono G. 1981. Contraction mechanism of helical muscles: experimental and theoretical analysis. J Submicrosc Cytol 13:253–66.

Lillie MA, Gosline JM. 2006. Tensile residual strains on the elastic lamellae along the porcine thoracic aorta. J Vasc Res 43:587–601.

Messenger JB, Nixon M, Ryan KP. 1985. Magnesium chloride as an anaesthetic for cephalopods. Comp Biochem Physiol 82:203–5.

Millman BM. 1967. Mechanism of contraction in Molluscan muscle. Amer Zool 7:583–91.

Moltschaniwskyj NA. 1994. Muscle tissue growth and muscle fibre dynamics in the tropical loliginid squid *Photololigo* sp. (Cephalopoda: Loliginidae). Can J Fish Aquat Sci 51: 830–5.

Moon TW, Hulbert WC. 1975. The ultrastructure of the mantle musculature of the squid *Symplectoteuthis oualaniensis*. Comp Biochem Physiol B Comp Biochem 52:145–9.

Olszewski-Jubelirer J. 2015. Obliquely-striated muscle is not just for super-elongation [M.S. thesis]. Chapel Hill: University of North Carolina.

Paps J, Baguñà J, Riutort M. 2009. Lophotrochozoa internal phylogeny: new insights from an up-to-date analysis of nuclear ribosomal genes. Proc R Soc B 276:1245–54.

Prosser CL. 1979. Evolution and diversity of nonstriated muscles. In: Bohr D, editor. Handbook of physiology, cardiovascular system II. Bethesda (MD): American Physiology Society. p. 635–70.

Prosser CL. 1982. Diversity of narrow-fibered and wide-fibered muscles. In: Twarog BM, Levine RJC, Dewey MM, editors. Basic biology of muscles: a comparative approach. New York (NY): Raven Press. p. 381–97.

Rack PMH, Westbury DR. 1969. The effects of length and stimulus rate on tension in the isometric cat soleus muscle. J Physiol 204:443–60.

Rosenbluth J. 1965. Ultrastructural organization of obliquely striated muscle fibers in *Ascaris lumbricoides*. J Cell Biol 25:495–515.

Rosenbluth J. 1967. Obliquely striated muscle. III. Contraction mechanism of *Ascaris* body muscle. J Cell Biol 34:15–33.

Rosenbluth J. 1972. Obliquely striated muscle. In: Bourne GH, editor. The structure and function of muscle, vol. 1. 2nd ed. New York (NY): Academic Press. p. 389–420.

Schneider CA, Rasband WS, Eliceiri KW. 2012. NIH Image to ImageJ: 25 years of image analysis. Nat Methods 9:671–5.

Shaffer JF, Kier WM. 2012. Muscular tissues of the squid *Doryteuthis pealeii* express identical myosin heavy chain isoforms: an alternative mechanism for tuning contractile speed. J Exp Biol 215:239–46.

Shaffer JF, Kier WM. 2016. Tuning of shortening speed in coleoid cephalopod muscle: no evidence for tissue-specific muscle myosin heavy chain isoforms. Invertebr Biol 135:3–12.

Thompson JT, Kier WM. 2006. Ontogeny of mantle musculature and implications for jet locomotion in oval squid *Sepioteuthis lessoniana*. J Exp Biol 209:433–43.

Thompson JT, Szczepanski JA, Brody J. 2008. Mechanical specialization of the obliquely striated circular mantle muscle fibres of the long-finned squid *Doryteuthis pealeii*. J Exp Biol 211:1463–74.

Thompson JT, Taylor KR, Gentile C. 2010a. Gradients of strain and strain rate in the hollow muscular organs of soft-bodied animals. Biol Lett 6:482–5.

Thompson JT, Bartol IK, Baksi AE, Li KY, Krueger PS. 2010b. The ontogeny of muscle structure and locomotory function in the long-finned squid *Doryteuthis pealeii*. J Exp Biol 213:1079–91.

Thompson JT, Shelton RM, Kier WM. 2014. The length–force behavior and operating length range of squid muscle vary as a function of position in the mantle wall. J Exp Biol 217:2181–92.
Thompson JT, LaValva SM, Loiacono MM. 2016. A multi-function muscle in squid. Biol Bull 231:225–35.
Ward DV, Wainwright SA. 1972. Locomotory aspects of squid mantle structure. J Zool Lond 167:437–49.
Williams CD, Salcedo MK, Irving TC, Regnier M, Daniel TL. 2013. The length–tension curve in muscle depends on lattice spacing. Proc R Soc B 280:20130697.

Supplemental Material

Shape, size, and structure affect obliquely striated muscle function in squid

by

Kari R. Taylor-Burt, William M. Kier, Julia Olszewski-Jubelirer, and Joseph T. Thompson.

Contents:

Table S1. List of individuals with number of jets involving mantle contraction or hyperinflation used in analysis

Stage	**Individual**	**Contraction** (n)	**Hyperinflation** (n)
Adult	1	28	9
	2	27	15
	3	8	0
	4	32	11
	5	34	11
	6	83	10
	7	46	15
	8	30	16
Hatchling	1	5	0
	2	2	0
	3	6	2
	4	6	0
	5	1	0
	6	4	1
	7	4	0
	8	9	0
	9	2	0
	10	3	0
	11	2	0
	12	2	0
	13	3	0
	14	4	0
	15	6	0
	16	6	3
	17	7	7

2. THE DISTRIBUTION OF OBLIQUELY STRIATED MUSCLES AMONG ANIMALS

Table S2: Invertebrate Phyla with Obliquely Striated Muscle

Phylum	**Reference**
Annelida	e.g., Rosenbluth (1968)
Brachiopoda	Kuga and Matsuno (1988)
Bryozoa	Bouligard (1966)
Chaetognatha	Duvert and Salat (1979)
Echinodermata	Carnevali et al. (1986)
Gastrotricha	Rieger et al. (1974); Teuchert (1974)
Gnathostomulida	Rieger and Mainitz (1977)
Mollusca	Amsellem and Nicaise (1980); Matsuno and Kuga (1989)
Nematoda	e.g., Rosenbluth (1965)
Nematomorpha	Eakin and Brandenburger (1974); Lanzavecchia et al. (1979)
Nemertea	Norenburg and Roe (1998)
Platyhelminthes	MacRae (1965), Ward et al. (1986)
Priapulida	Mattisson et al. (1974)
Rotifera	Bouligard (1966)
Sipunculida	DeEguileor and Valvassori (1977)
Tardigrada	Walz (1974)
Urochordata	Bone and Ryan (1974)

3. EXPLANATION OF THE MATLAB PROGRAM

The model was created in MATLAB r2014b (The Mathworks, Natick, MA) to calculate the force produced, based on the overlap between the thick and thin myofilaments. It first calculates the force for a sarcomere that is the length of one thick myofilament and increases the length incrementally by a unit equal to the distance between myosin heads until the sarcomere no longer produces force. To simplify the calculations, it considers a two-dimensional array of thick and thin filaments. The area of the two-dimensional array is held constant in order to simulate the essentially constant volume of an actual three-dimensional muscle fiber.

The following lengths are prescribed initially (See Fig. S1): thick myofilament (A), two thin myofilaments plus the width of a Z-body (b), bare zone of thick myofilament (BZ), myosin head spacing, number of myofilament pairs (n), and height of the sarcomere. The initial striation angle is prescribed. The area of the sarcomere is the product of the height and initial length of the sarcomere. The transverse distance between thin myofilaments (d) is calculated by dividing the height of the sarcomere by the number of filaments. The length of a line (designated p) connecting the Z-bodies on one side of the sarcomere is calculated by dividing the height of the sarcomere by the sine of the striation angle. The coordinates of the thick and thin myofilaments are calculated as indicated in Fig. S1.

Once the coordinates are determined, the overlap between the thick and thin filaments on each side of a thick filament and hence the number of cross-bridges interacting and force produced is calculated. At shorter sarcomere lengths, crossbridges are considered to not produce force if they are at a position where the thin filament from the opposite side of the sarcomere extends to their location, reflecting the hypothesis that thin myofilaments of opposite polarity interfere with cross-bridge formation (Gordon et al., 1966).

For each new sarcomere length, the height of the sarcomere was recalculated by dividing the area of the sarcomere by the new length. The angle of striation was then recalculated by taking the inverse since of the height of the sarcomere divided by p.

The total force at each length was divided by the maximum force the muscle produced (P_0), as is customary with empirically derived length-tension curves. The length was standardized by L_0, defined as the length at maximum force. The model allows exploration of the variables that are likely to have the greatest effect on length-tension behavior.

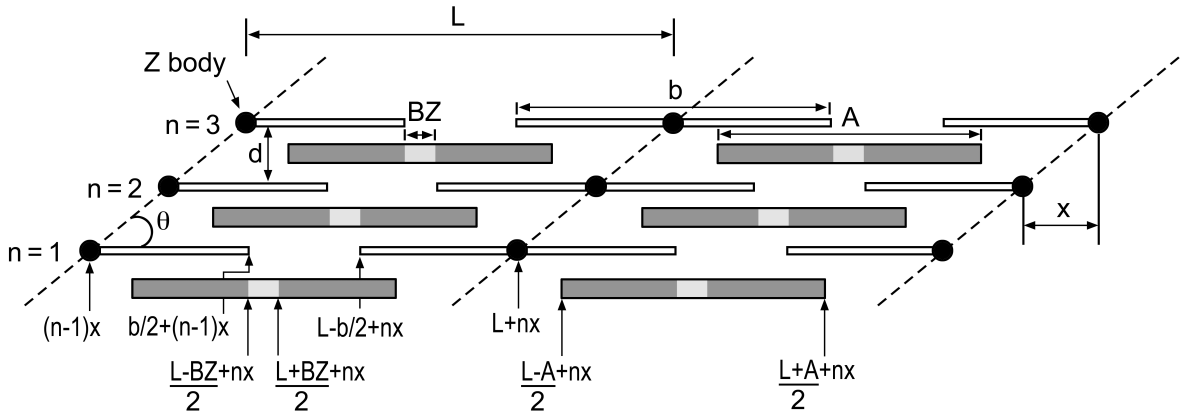

Figure S1 – Obliquely striated sarcomeres with dimensions considered in the model. L = sarcomere length, b= length of two thin myofilaments and one Z-body, x = the horizontal distance between two vertically adjacent thin myofilaments, d = distance beween two thin myofilaments, n = number of thin filament pairs, BZ = length of the bare zone, A = thick myofilament length, θ = angle of striation.

4. MATLAB PROGRAM FOR PREDICTING THE LENGTH-TENSION CURVE OF OBLIQUELY STRIATED MUSCLE

```
function[LTcurve]  = sarc_sim(angle,angle_changing,animate,moviename)


% assign filament dimensions in microns
A = 1.6; % length of the thick filament
I = 2.05; % length of two thin fiaments and a z-line or body
BZ = 0.20; % length of the bare-zone



mh_spacing = 0.02; % spacing between myosin
heads n = 30; % number of thin filaments
h_initial = 6; % initial height of the sarcomere
area = A*h_initial; % area is the initial length of the sarcomere (A)
times the intial height of the sarcomere (h)
p = h_initial/sin(angle/180*pi);  % other side of the parallelogram


% create figure for the
animation if animate
    fig = figure;
    hold on
    h1 = []; % dummy handle for some figure graphic
end


% create movie container if called
for if exist('moviename','var')
    mov = VideoWriter([moviename,'.avi']);
    open(mov);
end


% find the force at each sarcomere length
LF = zeros(round(2*I/mh_spacing)+1,2);  % create an array in which to store
Length and
Tension l = 1;
for L = A:mh_spacing:A+4*I
    h = area/L; % calculate the height of the sarcomere


    d = h/n; % calculate the distance between the filaments based on area
and length.



    % if the angle is changing, calculate the angle of
    striation if angle_changing
        theta = asin(h/p);
```

```
    else
        theta = angle/180*pi;
    end

    x = d/tan(theta); % calculate the lateral distance between the start
of thin filaments

    % create arrays to hold the locations of the filaments
    TFL = zeros(n-1,round((A-BZ)/2/mh_spacing)+1,2); % create an array to
hold the locations of the left myosin heads
    % fill in array for myosin
    heads for i = 1:n-1
        k = 1;
        for j = (L-A)/2 + x*i:mh_spacing:(L-BZ)/2  + x*i
            TFL(i,k,1) = j;
            TFL(i,k,2) = (i-
            1)*d; k = k+1;
       end
    en
    d

    TFR = zeros(n-1,round((A-BZ)/2/mh_spacing)+1,2); % create an array
to hold the locations of the right myosin heads
    % fill in array for myosin
    heads for i = 1:n-1
        k = 1;
        for j = (L+BZ)/2 + x*i:mh_spacing:(L+A)/2  + x*i
            TFR(i,k,1) = j;
            TFR(i,k,2) = (i-
            1)*d; k = k+1;
       end
    en
    d

    tfl = zeros(3,n); % create an array to hold the locations of the
left thin filaments
    % fill in array for the thin
    filaments for i = 1:n
        tfl(1,i) = (i-1)*x;
        tfl(2,i) = I/2 + (i-
        1)*x; tfl(3,i) = (i-
        1)*d;
    end

    tfr = zeros(3,n); % create an array to hold the locations of the
right thin filaments
    % fill in array for the thin
    filaments for i = 1:n
```

```
        tfr(1,i) = L-
        I/2+i*x; tfr(2,i) =
        L+i*x; tfr(3,i) =
        (i-1)*d;
    end


    % compare the arrays to calculate the force
    Fsumn = zeros(1,n); % create an empty array to count the force
produced by each filament set


    for i = 1:n-1 % for each filament
        for k = 1:round((A-BZ)/2/mh_spacing)+1  % along all possible
            positions if (tfl(1,i) <= TFL(i,k,1)) && (TFL(i,k,1) <= tfl(2,i))
                                                                    % if
            the
left myosin head overlaps with the left thin filament
                if (tfr(1,i) <= TFL(i,k,1)) && (TFL(i,k,1) <= tfr(2,i)) %
if they left myosin head overlaps with the right thin filament
                    Fsumn(i) = Fsumn(i); % keep the force the same
because the thin filaments are interfering with each other
                else
                    Fsumn(i) = Fsumn(i) + 1; % if the thin filaments do
not overlap and there is a left myosin head, add one to the force.
                end
            end

            if (tfl(1,i+1) <= TFL(i,k,1)) && (TFL(i,k,1) <= tfl(2,i+1)) %
 check the thin filament on the other side of the left myosin head
                if (tfr(1,i+1) <= TFL(i,k,1)) && (TFL(i,k,1) <= tfr(2,i+1))
                    Fsumn(i) = Fsumn(i);
                else
                     Fsumn(i) = Fsumn(i) + 1;
                end
            end



            if (tfr(1,i) <= TFR(i,k,1)) && (TFR(i,k,1) <= tfr(2,i)) %do the
same for the right myosin heads
                if (tfl(1,i) <= TFR(i,k,1)) && (TFR(i,k,1) <= tfl(2,i))
                    Fsumn(i) = Fsumn(i);
                else
                    Fsumn(i) = Fsumn(i) + 1;
                end
            end

            if (tfr(1,i+1) <= TFR(i,k,1)) && (TFR(i,k,1) <= tfr(2,i+1))
                if (tfl(1,i+1) <= TFR(i,k,1)) && (TFR(i,k,1) <= tfl(2,i+1))
                    Fsumn(i) = Fsumn(i);
```

```
                else
                    Fsumn(i)  = Fsumn(i)  + 1;
                end
            end

        end

    end
    % store the length and total force in the LF array
    LF(l,1)  = L;
    LF(l,2)  = sum(Fsumn);



    % create/update the animation if called for
    if animate
        if isempty(h1)  == false % delete graphics from the previous
            delete(h1);
            delete(h2);
            delete(h3);
            delete(h4);
            delete(h5);
        end

        % plot new components in the bottom panel
        subplot(2,1,1);
        hold on

        h1 = plot(TFL(1:n-1,1:round((A-BZ)/2/mh_spacing)+1,1),TFL(1:n-
1,1:round((A-BZ)/2/mh_spacing)+1,2),'g*');
        h2 = plot(TFR(1:n-1,1:round((A-BZ)/2/mh_spacing)+1,1),TFR(1:n-
1,1:round((A-BZ)/2/mh_spacing)+1,2),'g*');
        q = tfl(1:2,1:n);  w =
        tfl(3,1:n);  w(2,:) =
        tfl(3,1:n);  h3 =
        plot(q,w);



        r = tfr(1:2,1:n);  s =
        tfr(3,1:n);  s(2,:) =
        tfr(3,1:n);  h4 =
        plot(r,s);

        axis([0  A+2*I  0  h_initial]);
```

```
        % Adjust the length tension curve for P0 and L0
        [m,q] = size(LF);
        maxForce = max(LF(1:m,2));
        LTcurve(1:m,2) = LF(1:m,2)/maxForce;



        [r,c] = find(LTcurve == 1);
        [x,y] = size(r);
        L0 = sum(r(1:x))/x;


        LTcurve(1:m,1) = LF(1:m,1)/LF(round(L0),1);

        % plot new components in bottom panel
        subplot(2,1,2);
        hold on
        h5 = plot(LTcurve(1:m,1),LTcurve(1:m,2),'g*');
        axis([0 4 0 1])

        % add frame to the movie if we're creating one
        if exist('moviename','var')
            % Write each frame to the file
            currFrame = getframe(gcf);
            writeVideo(mov,currFrame);
        end
    else
        % Adjust the length tension curve for P0 and L0
        [m,q] = size(LF);
        maxForce = max(LF(1:m,2));
        LTcurve(1:m,2) = LF(1:m,2)/maxForce;



        [r,c] = find(LTcurve == 1);
        [x,y] = size(r);
        L0 = sum(r(1:x))/x;


       LTcurve(1:m,1) = LF(1:m,1)/LF(round(L0),1);
    en
    d


    pause(.01) % slight pause so the figure animation gets displayed

    if LF(l,2) == 0 % if the force is 0, stop the program
        break
    end
    l = l+1;

end
```

```
% close the movie if we created one
if exist('moviename','var')
    close(mov);
end



end
```

5. REFERENCES CITED

Amsellem J, Nicaise G. 1980. Ultrastructural study of muscle cells and their connections in the digestive tract of *Sepia officinalis*. J. Submicrosc. Cytol. 12: 219-231.

Bone Q, Ryan KP. 1974. On the structure and innervation of the muscle bands of *Dolium* (Tunicata: Cyclomyaria). Proc. R. Soc. Lond. B. 187: 315-327.

Bouligard Y. 1966. La disposition des myofilaments chez une annélide polychète. J. Microscopie. 5: 305-322.

Carnevali MDC, Saita A, Fedrigo A. 1986. An unusual Z-system in the obliquely striated muscles of crinoids: three-dimensional structure and computer simulations. J. Muscle Res. Cell Motil. 7: 568-578.

DeEguileor M, Valvassori R. 1977. Studies on the helical and paramyosinic muscles. VII. Fine structure of body wall muscles in *Sipunculus nudus*. J. Submicrosc. Cytol. 9: 363-372.

Duvert M, Salat C. 1979. Fine structure of muscle and other components of the trunk of *Sagitta setosa* (chaetognath). Tissue Cell. 11: 217-230.

Eakin RM, Brandenburger JL. 1974. Ultrastructural features of a Gordian worm (Nematomorpha). J. Ultrastruct. Res. 46: 351-374.

Gordon AM, Huxley AF, Julian FJ. 1966. The variation in isometric tension with sarcomere length in vertebrate muscle fibres. J. Physiol. 184; 170-192.

Kuga H, Matsuno A. 1988. Ultrastructural investigations on the anterior adductor muscle of a brachipoda, *Lingula unguis*. Cell Struct. Function. 13: 271-279.

Lanzavecchia G, Valvassori R, De Eguileor M, Lanzavecchia Jr. P. 1979. Three-dimensional reconstruction of the contractile system of the Nematomorpha muscle fiber. J. Ultrastruct. Res. 66: 201-223.

MacRae EK. 1965. The fine structure of muscle in a marine turbellarian. Z. Zellforsch. 68: 348-362.

Matsuno A, Kuga H. 1989. Ultrastructure of muscle cells in the adductor of the boring clam *Tridacna crocea*. J. Morphol. 200: 247-253.

Mattisson A, Nilsson S, Fänge R.1974. Light microscopical and ultrastructural organization of muscles of *Priapulus caudatus* (Priapulida) and their responses to drugs with phylogenetic remarks. Zool. Scr. 3: 209-218.

Norenburg JL, Roe P. 1998. Observations on musculature in pelagic nemerteans and on pseudostriated muscle in nemerteans. Hydrobiologia. 356: 109-120.

Rieger RM, Ruppert E, Rieger GE, Schoepfer-Sterrer C. 1974. On the fine structure of gastrotrichs with description of *Chordodasys antennatus* sp.n. Zool. Script. 3: 219-237.

Rieger RM, Mainitz M. 1977. Comparative fine structure study of the body wall in Gnathostomulida and their phylogenetic position between Platyhelminthes and Aschelminthes. Z. Zool. Syst. Evol. 15: 9-35.

Rosenbluth J. 1965. Ultrastructural organization of obliquely striated muscle fibers in *Ascaris lumbricoides*. J. Cell Biol. 25: 495-515.

Rosenbluth J. 1968. Obliquely striated muscle. IV. Sarcoplasmic reticulum, contractile apparatus, and endomysium of the body muscle of a polychaete, *Glycera,* in relation to its speed. J. Cell Biol. 36: 245-259.

Teuchert G. 1974. Light and electron microscopical features of the muscular system from *turbanella cornuta* (Gastrotricha, Macrodaysoidea). Mikrofauna des Meeresbodens. 39: 1-26.

Walz B. 1974. The fine structure of somatic muscles of Tardigrada. Cell Tissue Res. 149: 81-89.

Ward SM, McKerr G, Allen JM. 1986. Structure and ultrastructure of muscle systems within *Grillotia erinaceus* metacestodes (Cestoda, Trypanorhyncha). Parasitology. 93: 587-597.